

Influence of birefringence on polarization resolved nonlinear microscopy and collagen SHG structural imaging

D. Aït-Belkacem, A. Gasecka, F. Munhoz, S. Brustlein, and S. Brasselet*

*Institut Fresnel, CNRS, Aix-Marseille Université, Ecole Centrale Marseille, Campus de St Jérôme, 13013 Marseille, France MOSAIC
Domaine universitaire St Jérôme,
13397 Marseille Cedex 20, France
*sophie.brasselet@fresnel.fr*

Abstract: We analyze the influence of the anisotropy of molecular and biological samples on polarization resolved nonlinear microscopy imaging. We show in particular the detrimental influence of birefringence on Second Harmonic Generation (SHG) and Two-Photon Excited Fluorescence (TPEF) polarization resolved microscopy imaging, which, if not accounted for, can lead to an erroneous determination of the sample properties and thus to a misinterpretation of the read-out information. We propose a method to measure this birefringence and account for this effect in nonlinear polarization resolved experiments.

© 2010 Optical Society of America

OCIS codes: (180.4315) Nonlinear microscopy; (190.1900) Diagnostic applications of nonlinear optics.

References and links

1. J. Gannaway and C. J. R. Sheppard, "Second harmonic imaging in the scanning optical microscope," *Opt. Quantum Electron.* **10**, 435–439 (1978).
2. I. Freund, M. Deutsch, and A. Sprecher, "Connective tissue polarity. Optical second-harmonic microscopy, crossed-beam summation, and small-angle scattering in rat-tail tendon," *Biophys. J.* **50**, 693–712 (1986).
3. M. Flörshheimer, C. Radüge, H. Salmen, M. Bösch, R. Terbrack, and H. Fuchs, "In-situ imaging of Langmuir monolayers by second-harmonic microscopy," *Thin Solid Films* **284**, 659–662 (1996).
4. L. Moreaux, O. Sandrea, and J. Mertz, "Membrane Imaging by Second Harmonic Generation Microscopy," *J. Opt. Soc. Am. B* **17**, 1685–1689 (2000).
5. P. J. Campagnola, A. C. Millard, M. Terasaki, P. E. Hoppe, C. J. Malone, and W. A. Mohler, "3-Dimensional High-Resolution Second Harmonic Generation Imaging of Endogenous Structural Proteins in Biological Tissues," *Biophys. J.* **81**, 493–508 (2002).
6. D. A. Dombeck, K. A. Kasischke, H. D. Vishwasrao, M. Ingelsson, B. T. Hyman, and W. W. Webb, "Uniform polarity microtubule assemblies imaged in native brain tissue by second-harmonic generation microscopy," *Proc. Natl. Acad. Sci. U.S.A.* **100**, 7081 (2003).
7. M. Strupler, M. Hernest, C. Fligny, J. L. Martin, P.-L. Tharaux, and M. C. Schanne-Klein, "Second Harmonic Microscopy to Quantify Renal Interstitial Fibrosis and Arterial Remodeling," *J. Biomed. Opt.* **13**, 054041 (2008).
8. O. Nadiarnykh, R. LaComb, M. Brewer, and P. J. Campagnola, "Second Harmonic Generation Imaging Microscopy of Ovarian Cancer," *Biophys. J.* **94**, 4504–4514 (2008).
9. S. W. Teng, H. Y. Tan, J. L. Peng, H. H. Lin, K. H. Kim, W. Lo., Y. Sun, W. C. Lin, S. J. Lin, S. H. Jee, P. T. C. So, and C. Y. Dong, "Multiphoton autofluorescence and second-harmonic generation (SHG) imaging of ex-vivo porcine eye," *Invest. Ophthalmol. Vis. Sci.* **47**, 1216–1224 (2006).

10. E. Ralston, B. Swaim, M. Czapiga, W. L. Hwu, Y. H. Chien, M. G. Pittis, B. Bembi, O. Schwartz, P. Plotz, and N. Raben, "Detection and imaging of non-contractile inclusions and sarcomeric anomalies in skeletal muscle by second harmonic generation combined with two-photon excited fluorescence," *J. Struct. Biol.* **162**, 500–508 (2008).
11. D. Axelrod, "Carbocyanine dye orientation in red cell membrane studied by microscopic fluorescence polarization," *Biophys. J.* **26**, 557–573 (1979).
12. J. Borejdo and S. Burlacu, "Measuring Orientation of Actin Filaments within a Cell: orientation of Actin in Intestinal Microvilli," *Biophys. J.* **65**, 300–309 (1993).
13. M. Flörsheimer, M. Bösch, C. Brillert, M. Wierschem, and H. Fuchs, "Second-harmonic microscopy - a quantitative probe for molecular surface order," *Adv. Mater.* **9**, 1061–1065 (1997).
14. C. Anceau, S. Brasselet, and J. Zyss, "Local orientational distribution of molecular monolayers probed by nonlinear microscopy," *Chem. Phys. Lett.* **411**, 98–102 (2005).
15. P. Stoller, B. M. Kim, A. M. Rubenchik, K. M. Reiser, and L. B. Da Silva, "Polarization-dependent optical second harmonic imaging of a rat-tail tendon," *J. Biomed. Opt.* **7**, 205–214 (2000).
16. P. Stoller, K. M. Reiser, P. M. Celliers, and A. M. Rubenchik, "Polarization-Modulated Second Harmonic Generation in Collagen," *Biophys. J.* **82**, 3330–3342 (2002).
17. T. Yasui, K. Sasaki, Y. Tohno, and T. Araki, "Tomographic imaging of collagen fiber orientation in human tissue using depth-resolved polarimetry of second-harmonic-generation," *Opt. Quantum Electron.* **37**, 1397–1408 (2005).
18. R. M. Williams, W. R. Zipfel, and W. W. Webb, "Interpreting Second-Harmonic Generation Images of Collagen I Fibrils," *Biophys. J.* **88**, 1377–1386 (2005).
19. S. Yen, W. L. Chen, H. Y. Wu, F. C. Li, W. Lo, S. J. Lin, S. H. Jee, Y. F. Chen, P. T. C. So, and C. Y. Dong, "Collagen Thermal denaturation study with high resolution second harmonic generation imaging and polarization optical microscopy," *Biophys. J.* **91**, 2620–2625 (2006).
20. F. Tiaho, G. Recher, and D. Rouède, "Estimation of helical angles of myosin and collagen by second harmonic generation imaging microscopy," *Opt. Express* **15**, 4054–4065 (2007).
21. C. Odin, Y. Le Grand, A. Renault, L. Gailhouste, and G. Baffet, "Orientation fields of nonlinear biological fibrils by second harmonic generation microscopy," *J. Microsc.* **229**, 32–38 (2008).
22. S. Psilodimitrakopoulos, S. I. C. O. Santos, I. Amat-Roldan, A. K. N. Thayil, D. Artigas, and P. Loza-Alvarez, "In vivo, pixel-resolution mapping of thick filaments' orientation in nonfibrillar muscle using polarization-sensitive second harmonic generation microscopy," *J. Biomed. Opt.* **14**, 014001 (2009).
23. A. Gasecka, T.-J. Han, C. Favard, B. R. Cho, and S. Brasselet, "Quantitative imaging of molecular order in lipid membranes using two-photon fluorescence polarimetry," *Biophys. J.* **97**, 2854–2862 (2009).
24. A. Gasecka, L.-Q. Dieu, D. Bruehvilier, and S. Brasselet, "Probing molecular order in zeolite L inclusion compounds using two-photon fluorescence polarimetric microscopy," *J. Phys. Chem. B* **114**, 4192–4198 (2010).
25. V. Le Floch, S. Brasselet, J.-F. Roch, and J. Zyss, "Monitoring of orientation in molecular ensembles by polarization sensitive nonlinear microscopy," *J. Phys. Chem. B* **107**, 12403–12410 (2003).
26. S. Brasselet, V. Le Floch, F. Treussart, J.-F. Roch, J. Zyss, E. Botzung-Appert, and A. Ibanez, "In situ diagnostics of the crystalline nature of single organic nanocrystals by nonlinear microscopy," *Phys. Rev. Lett.* **92**, 207401–207405 (2004).
27. K. Komorowska, S. Brasselet, J. Zyss, L. Pourlsen, M. Jazdyk, H. J. Egelhaaf, J. Gierschner, and M. Hanack, "Nanometric scale investigation of the nonlinear efficiency of perhydrotriphenylene inclusion compounds," *Chem. Phys.* **318**, 12–20 (2005).
28. S. Brasselet, and J. Zyss, "Nonlinear polarimetry of molecular crystals down to the nanoscale," *C. R. Physique* **8**, 165–179 (2007).
29. P. Schön, F. Munhoz, A. Gasecka, S. Brustlein, and S. Brasselet, "Polarization distortion effects in polarimetric two-photon microscopy," *Opt. Express* **16**, 20891–20901 (2008).
30. B. Richards, and E. Wolf, "Electromagnetic Diffraction in Optical Systems. II. Structure of the Image Field in an Aplanatic System," *Proc. R. Soc. London Ser. A* **253**, 358–379 (1959).
31. E. Y. S. Yew, and C. R. J. Sheppard, "Effects of axial field components on second harmonic generation microscopy," *Opt. Express* **14**, 1167–1174 (2006).
32. N. Sandeau, L. L. Xuan, D. Chauvat, C. Zhou, J. F. Roch, and S. Brasselet, "Defocused imaging of second harmonic generation from a single nanocrystal," *Opt. Express* **15**, 16051–16060 (2007).
33. P. Schön, M. Behrndt, D. Ait-Belkacem, H. Rigneault, and S. Brasselet, "Polarization and Phase Pulse Shaping applied to Structural Contrast in Nonlinear Microscopy Imaging," *Phys. Rev. A* **81**, 013809 (2010).
34. D. Lara and C. Dainty, "Axially resolved complete Mueller matrix confocal microscopy," *Appl. Opt.* **45**, 1917–1930 (2006).
35. C. E. Bigelow, and T. H. Foster, "Confocal fluorescence polarization microscopy in turbid media: Effects of scattering-induced depolarisation," *J. Opt. Soc. Am. A* **23**, 2932 (2006).
36. I. Ledoux, C. Lepers, A. Prigaud, J. Badan, and J. Zyss, "Linear and nonlinear optical properties of N-4-nitrophenyl L-prolinol single crystals," *Opt. Commun.* **80**, 149–154 (1990).
37. F. P. Bolin, L. E. Preuss, R. C. Taylor, and R. J. Ferenc, "Refractive index of some mammalian tissues using a

- fiber optic cladding method," Appl. Opt. **28**, 2297–2303 (1989).
38. D. T. Poh, "Examination of refractive index of human epidermis in-vitro and in-vivo.," Proc. Inter. Conf. Lasers. **96**, 118–125 (1996).
-

1. Introduction

Since its first developments [1–3] and its introduction in bio-imaging [4–6], second harmonic generation (SHG) microscopy is now widely used to image ordered biomolecular assemblies in complex samples at depths reaching a few hundreds of micrometers. Coherent SHG occurring naturally in non-centrosymmetric structures such as collagen [2], skeletal muscles [5] and microtubules [6], is today exploited as a functional contrast [7, 8], possibly in conjunction with Two-Photon Excited Fluorescence (TPEF) [9, 10], with the ultimate goal of developing diagnostics of pathological effects related to tissues and cell architecture.

In addition to their unique imaging capabilities, these contrasts are dependent on the incident light polarization state, providing an interesting way to probe molecular orientation and disorder. Structural information, from membrane architecture and proteins aggregates to biopolymers and tissue assemblies, is a key parameter in a large variety of biological phenomena. Polarization probe imaging has been exploited a long time ago in fluorescence [11, 12] and SHG [13, 14] in ordered molecular samples. Its extension to SHG in tissues leads to a large amount of current studies [15–22].

Recent works in polarization resolved nonlinear microscopy (or nonlinear polarimetry) have pointed out the need to rely on a variable state of incident polarization to retrieve relevant information on the sample structure. In fluorescence, measuring the signal from a continuous variation of the incident linear polarization state circumvents the limitations of the traditional fluorescence anisotropy imaging, which explores a limited number of polarization states and therefore requires *a priori* knowledge information on the studied system [11, 12]. TPEF polarimetry has shown in particular its ability to reveal non-ambiguous information on molecular angular distributions in cell membranes and crystals [23, 24], with a typical 300nm lateral resolution.

In SHG, polarimetry is particularly relevant since the complex nature of the probed $\chi^{(2)}$ tensor requires multiple polarization coupling. SHG polarimetry imaging has allowed retrieving molecular orientation and order information in molecular materials [14, 25] and crystals down to the nanometric size [26–28], as well as collagen and muscle structural quantitative information in tissues [15–22].

Although polarimetry microscopy imaging is a powerful technique, relevant information can be retrieved only if particular care is brought on the possible polarization distortions occurring in the instrument. The degree of ellipticity appearing from reflections on mirrors and dichroic mirrors can lead to a deformation of the retrieved information, in particular when using the epi-geometry [29]. In addition, the excitation and detection polarization are scrambled due to the use of high numerical aperture objectives [11]. Finally an extra coupling along the propagation direction appears to be non-negligible when using high aperture focusing [30]. These different polarization distortion factors have been thoroughly addressed and can be readily accounted for in microscopy polarization analysis [25, 31–33].

Apart from these instrumental effects, other polarization distortions can originate from the sample itself, especially when propagating through micrometric scale depths. Scattering involves more specifically depolarization, which can be identified and eventually corrected for by measuring depolarization properties using for instance the Mueller matrix formalism [34, 35]. In this work we focus on birefringence, which can be non-negligible and even sometimes significant in crystalline [36] and biological samples, in particular from fibrillar structures such as collagen even at a few micrometer depths [37, 38]. Birefringence, which introduces a phase

shift in the input field polarization state between optical axes of *a priori* unknown orientations, can lead to erroneous deductions on the measured properties such as SHG nonlinear tensorial components. We show that this effect in collagen, which has been so far evoked in only a few works in nonlinear polarized microscopy [16], and ignored in most of the previous polarization resolved studies [17, 20–22], can be detrimental to the measured signals. In this work, we analyze the effect of birefringence in polarimetric TPEF and SHG microscopy applied to anisotropic samples widely studied in molecular and biological sciences. Although these contrasts are chosen for the possibility to combine them on the same microscope, the present study can be easily adapted to one-photon fluorescence or other nonlinear processes.

2. Effect of birefringence on polarimetric microscopy imaging

The nonlinear polarimetric microscope used in this work has been described in previous works [23, 26]. The excitation light source is a tunable Ti:Sapphire laser (Chameleon, Coherent) that delivers 150 fs pulses at a repetition rate 80 MHz. The incident wavelength is set at 800nm (for SHG) and 840nm (for TPEF) with a typical averaged power of a few mWs. The laser beam is reflected by a dichroic mirror and focused on the sample by a relatively low Numerical Aperture (NA) objective ($\times 40$, 0.6 NA), in order to discriminate high aperture focusing effects from the present birefringence effect study. The backward emitted signal is collected by the same objective and directed to a polarization beamsplitter that separates the beam towards two avalanche photodiodes. Images are performed by scanning the sample on a piezoelectric stage, which allows precise location of polarimetric measurement points. The linear polarization of the incident laser beam is continuously rotated in the sample plane by an achromatic half waveplate mounted on a step rotation motor at the entrance of the microscope. For each value of the polarization angle α (relative to X), the emitted signal is recorded on the two perpendicular directions X (I_X) and Y (I_Y) defining the sample plane [Fig. 1(a), 1b)]. In order to measure locally the birefringence properties of the studied sample, we implemented on the same microscope a forward polarized detection identical to the backward set-up, the detected signal being the incident fundamental beam at the input ω frequency. Upon rotation of the incident linear polarization, the ellipticity occurring from the sample birefringence is expected to strongly modify the polarimetric dependence of the measured signal through the whole sample thickness L [Fig. 1(c)]. At last, polarization distortions dichroism and ellipticity occurring from the mirrors reflection are preliminarily characterized following a calibration procedure using a fluorescent solution as described in [29].

For both the TPEF and SHG contrasts, varying the incident polarization angle α allows retrieving information on the unknown molecular angular distribution denoted $f(\theta, \phi, \psi)$, with (θ, ϕ, ψ) the Euler set of angles defining the molecular frame orientation in the sample. In what follows, we discard the ψ angle since cone-shape distributions are considered where only the (θ, ϕ) angle components are relevant by cylindrical symmetry, as often applied to biological media such as in cell membranes [11] and fibrillar structures [2]. Nevertheless this model can be extended to more general distribution functions.

The TPEF polarimetric signal measured from a molecular ensemble within an orientational distribution $f(\theta, \phi)$ (with (θ, ϕ) the molecular dipole orientation angle), analyzed along a given polarization state $I = (X, Y)$, can be expressed as the incoherent sum over individual fluorescent intensities [23, 25]:

$$I_{I=(X,Y)}^{TPEF}(\alpha) = \int_0^{2\pi} \int_0^\pi |\vec{\mu}_{abs}(\theta, \phi) \cdot \vec{E}(\alpha)|^4 |\vec{\mu}_{em}(\theta, \phi) \cdot \vec{I}|^2 f(\theta, \phi) \sin \theta d\theta d\phi \quad (1)$$

where $\vec{\mu}_{abs}$ is the molecular absorption dipole, and $\vec{\mu}_{em}$ is its emission dipole, both fixed relative to the molecular microscopic frame. $\vec{E}(\alpha)$ the incident linear polarization state vector oriented

with an angle α relative to X . This expression, written in the planar wave approximation, assumes a small collection angle of the fluorescence radiation. In the case of a high aperture collection angle, the $|\vec{\mu}_{em}(\theta, \phi) \cdot \vec{I}|^2$ emission contribution in Eq. (1) has to be replaced by the $J_I(\theta, \phi)$ corrected function, previously introduced to account for the broad range of collection angles within a high numerical aperture (NA) objective [11]. In the present work, the use of a low-NA objective (NA=0.6) allows considering the planar wave approximation to be relevant [29, 33].

In the case of SHG, the signal results from the coherent radiation of nonlinear molecular induced dipoles, induced in the focal spot of the objective. This leads to the following SHG intensity measured along the $I = (X, Y)$ polarization analysis direction:

$$I_{I=(X,Y)}^{SHG}(\alpha) = \left| \sum_{J,K} \chi_{IJK}^{(2)} E_J^\omega(\alpha) E_K^\omega(\alpha) \right|^2 \quad (2)$$

with $\chi_{IJK}^{(2)}$ the macroscopic nonlinear SHG tensorial coefficients with $(I, J, K) = (X, Y, Z)$. This expression is written in the planar wave approximation but can nevertheless be completed for high NA [31, 33]. The $\chi_{IJK}^{(2)}$ coefficients are related to the angular molecular distribution in the focal spot of the microscope $f(\theta, \phi)$ following expressions developed previously [14, 20–22, 25].

Note that due to the small size of the focal volume relative to the nonlinear coherent lengths, the phase matching relations occurring usually at a large propagation distance are not accounted for here.

In both expressions [Eqs. (1) and (2)], the optical field $\vec{E}(\alpha)$ is expressed at the dipoles positions (either fluorescent or nonlinear induced) in the focal spot of the microscope objective, at a given depth d from the sample surface [Fig. 1(c)]. In anisotropic samples where this incident field undergoes a birefringence retardation, its expression has to be re-written in order to account for the consequent polarization distortions. In the present work, we consider that the object projection in the sample plane is uni-axial, which is consistent with a cylindrical-symmetry distribution lying in the (X, Y) plane as mentioned above. This is also relevant in most of the systems imaged in nonlinear microscopy. In the other cases, only a picture of the sample projection is possible since the optical coupling is limited to the X and Y polarization directions. Denoting Θ_b the angle between the X macroscopic axis and the fast optical axis X_b of this object [Fig. 1(b)], and Φ_b the phase shift between its fast and slow optical axes, then the new expression of the optical field polarization state at the focal depth distance d is, in the planar wave approximation:

$$\begin{bmatrix} E_X(Z=d) \\ E_Y(Z=d) \end{bmatrix} = \begin{bmatrix} \exp(i\Phi_b(d)) \cdot \cos \Theta_b & -\sin \Theta_b \\ \exp(i\Phi_b(d)) \cdot \sin \Theta_b & \cos \Theta_b \end{bmatrix} \cdot \begin{bmatrix} \cos \Theta_b & \sin \Theta_b \\ -\sin \Theta_b & \cos \Theta_b \end{bmatrix} \cdot \begin{bmatrix} E_X^0(\alpha) \\ E_Y^0(\alpha) \end{bmatrix} \quad (3)$$

with $E_{X,Y}^0$ the optical field polarization components in the macroscopic (X, Y) frame at the sample surface ($Z=0$) [Fig. 1(c)], and $\Phi_b(d) = \frac{2\pi}{\lambda} \Delta n \cdot d$, with λ the incident wavelength and Δn the refractive index difference between the fast and slow axis of the object in the sample plane.

In addition to its effect on the incident excitation field, the birefringence also affects the detected signal, which propagates back in the sample in the case of a backward detection. A similar approach as above can be implemented to account for this effect, assuming that the same Δn value applies to both incident and emitted wavelengths (this is the case if no resonance is involved). The relation between the macroscopic emission dipole components (either occurring from a TPEF process or an induced nonlinear SHG process) at the focal depth d and at the

exit of the sample ($Z = 0$) follows the same equation as in Eq. (3), introducing the detection wavelength in the expression of Φ_b .

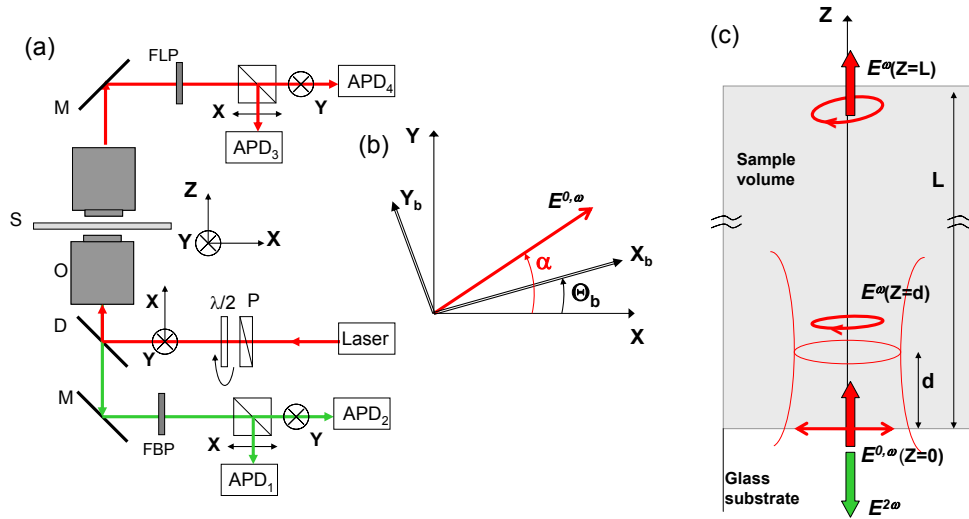


Fig. 1. (a) Experimental set-up. D: dichroic mirror, APD: avalanche photodiodes, P: polarizer, M: mirror, S : sample, FLP : long pass filter, FBP : band pass filter. (b) Definition of the input polarization angle α and the birefringence slow axis direction θ_b relative to X . (c) Experimental configuration: an incident linear polarized field at the ω frequency is focused at a distance d from the sample surface in the optical axis Z direction. The transmitted fields at ω at both the distance d and the sample output distance L are elliptical if the sample is birefringent. The emitted field (fluorescence or 2ω for SHG) is measured in the epi direction.

3. In situ characterization of the sample local birefringence

Equation (3) shows that for a varying angle α of the incident polarization $\vec{E}(\alpha)$, the sample birefringence parameters can be deduced from a polarimetric measurement performed in the forward direction for the ω frequency of the excitation field [Fig. 1(a)]. In such geometry, the field propagates through the whole thickness of the sample L and therefore $\Phi_b(L)$ is measured. Theoretical polarimetric responses of the incident intensity $I_X^\omega(\alpha)$ are depicted in Fig. 2(a) in a polar representation, for a sample tilt angle of the optical axis of $\Theta_b = 30^\circ$, and for different birefringence phase shifts. If no birefringence occurs in the sample, the polarization response is a $\cos^2 \alpha$ two-lobes pattern with a maximum intensity along X ($\alpha = 0^\circ$) and a vanishing intensity along Y ($\alpha = 90^\circ$). In the presence of birefringence, this pattern tends to open (no extinction occurs anymore) and rotates progressively when Φ_b increases. Similar responses are expected for I_Y^ω , rotated by 90° with respect to I_X^ω .

As seen in Fig. 2(b), experimental $I_{X,Y}^\omega$ polarimetric measurements performed at a given position on a collagen type I fiber of roughly $70\text{-}100\mu\text{m}$ thickness exhibit such behavior (the sample preparation details can be found in the SHG section below). Figure 2(c) shows a map of the mean square error to the theoretical model [Eq. (3)] as a function of the deduced parameters. The minima of the fitting error can be found for Θ_b with a $\pi/2$ periodicity, and $\Phi_b(L)$

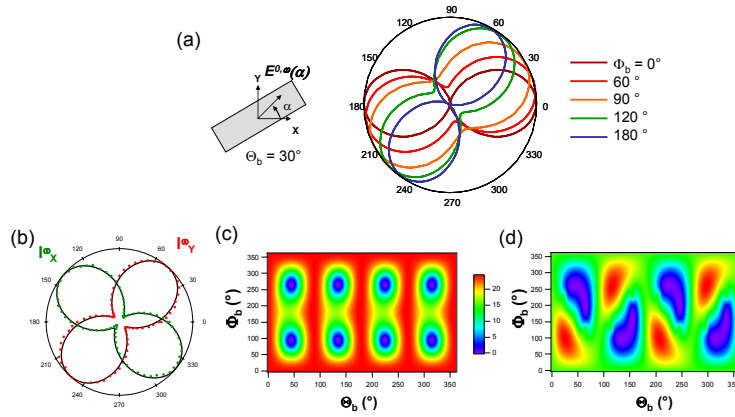


Fig. 2. (a) Theoretical linear polarimetric responses I_X^ω through a birefringent sample at different values of Φ_b , for an optical axis tilt of $\Theta_b = 30^\circ$. (b) Experimental linear polarimetric responses $I_{X,Y}^\omega$ (dots) through a collagen type I fiber from a rat-tail tendon, oriented at 45° relative to X . The fit (black lines) uses the model detailed in the text. (c,d) Maps of the mean square error between fitted and experimental intensities : (c) with no dichroic mirror polarization distortion, (d) with polarization distortions (dichroism factor $\gamma = 0.043$, ellipticity factor $\delta = 55^\circ$, with the notations of [29]). Fit solutions : $\Theta_b = 44^\circ$ and $\Phi_b = 97^\circ$.

with a π periodicity, the periodicity being consistent with the fact that this technique does not discriminate the fast or slow axes of the system (this indetermination does not affect the results for the detected signals, as seen below). Note that accounting for the ellipticity and dichroism introduced by the dichroic mirror as mentioned in [29] leads to a slight modification of the fit solutions [Fig. 2(d)] which has to be ultimately introduced in the models for TPEF or SHG contrasts as detailed below. Figure 2(d) shows in particular that introducing the instrumental distortions in the data analysis is crucial before any sample analysis. The birefringence parameters $\Phi_b(L)$ and Θ_b determined from the fit of [Fig. 2(b)] shows that (i) Θ_b lies roughly along the observed collagen fiber orientation (here 45°) and (ii) the measured birefringence phase shift $\Phi_b(L) = 97^\circ$ can be used to deduce the approximate sample thickness L at the measured sample location. Assuming $\Phi_b \approx 1.35^\circ/\mu\text{m}$ ($\Delta n \approx 0.003$ [37, 38]) between the long axis of collagen fibers and their orthogonal direction, this measurement leads to $L \approx 72\mu\text{m}$, which is reasonable in the studied sample.

In the following sections, both TPEF and SHG contrasts are studied with known instrumental factors, Θ_b and Φ_b being introduced as fitting parameters in anisotropic molecular assemblies. Such systems can be viewed as an ensemble of excitation/emission dipoles lying within a cylindrical symmetry angular distribution $f(\theta, \phi)$. This distribution is most generally modeled by a cone shape of given aperture and mean direction angles. This model has been applied to a large number of situations in polarization resolved fluorescence such as in labeled lipid membranes [11], labeled Actin fibers [12] or disordered molecular crystals [28, 33] as well as for SHG in collagen where the traditionally used C_6 crystal point group model leads to a nonlinear tensor equivalent to that of a cone [2, 20–22]. In such uni-axial samples the molecular order imposes an anisotropy along the main axis that can lead to non-negligible birefringence.

4. TPEF polarization resolved microscopy in crystalline samples

In order to visualize the effect of birefringence on TPEF, a model is applied to a cone lying in the (X, Y) plane, which main orientation φ_0 relative to X also corresponds to the optical axis of the uni-axial object. Figure 3 shows the effect of birefringence on the I_X and I_Y TPEF polarimetric response in a system of large cone aperture. An increasing birefringence leads to a deformation of the polarimetric polar plots, in particular when the optical axis is away from the experimental projection axes X or Y . This would clearly lead to a misinterpretation of the polarimetric data, even for slight birefringence phase shifts. In particular for large values of Φ_b , the polarimetric data resemble those of a much smaller cone aperture than what is actually.

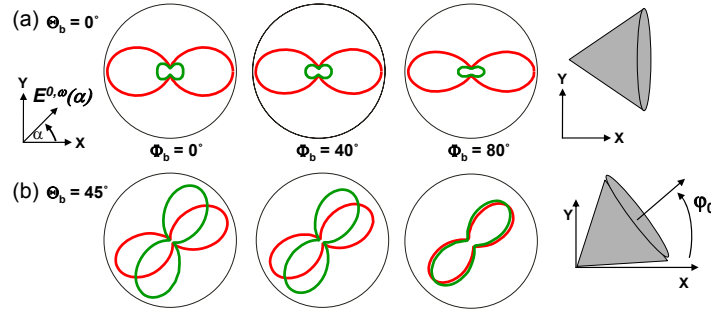


Fig. 3. Theoretical TPEF polarimetric responses I_X^{TPEF} (red) and I_Y^{TPEF} (green) for a molecular distribution within a large cone aperture (half angle 50°), for different orientations φ_0 of the cone in the (X, Y) frame (corresponding here also to the optical axis orientation Θ_b). (a) $\varphi_0 = \Theta_b = 0^\circ$ and (b) $\varphi_0 = \Theta_b = 45^\circ$, with different values of the birefringence phase shift Φ_b .

Experimental TPEF polarimetric data are shown in Fig. 4 on a 1D macroscopic uni-axial molecular co-crystal of Perhydrotriphenylene(PHTP)-4-Dimethylamino-40-nitrostilbene(DANS) described in a previous work [27]. In this crystal the birefringence is non-negligible, which is particularly visible when the crystal is tilted [Fig. 4(c)]. The birefringence phase shift deduced from the fit of I_Y^ω is only indicative since a large thickness (about $500 \mu\text{m}$) is crossed in the forward direction, and therefore many π phase shift periods are expected. To fit the TPEF polarimetric data, the molecular 1D distribution is modeled by a cone of infinitely small aperture angle (dirac function) oriented along the main axis of the crystal by an angle φ_0 relative to X . All angles φ_0 , Θ_b and Φ_b , are used as fitting parameters. The fit, which is clearly improved by accounting for birefringence [Fig. 4(e), 4(f)], leads to values consistent with both the tilt angle of the crystal ($\varphi_0 \approx 135^\circ$) and a large birefringence. At a penetration depth of $5 \mu\text{m}$, the fitted birefringence phase shift leads to $\Delta n \approx 0.04$, which is relevant in such system where Δn values ranging between 0.001 and 0.8 have been reported in molecular crystals [36]. Note that the measured birefringence value is averaged over the excitation volume of the objective, which introduces an error margin on the penetration depth value and therefore on the Δn determination. In addition, the difference between φ_0 and Θ_b found when fitting I^ω and I^{TPEF} might be due to a slight heterogeneity of the crystal main axis orientation through its large thickness. Nevertheless, if the birefringence effect is not accounted for in the TPEF polarimetric fit, the quality of the fit is considerably reduced [Fig. 4(f)].

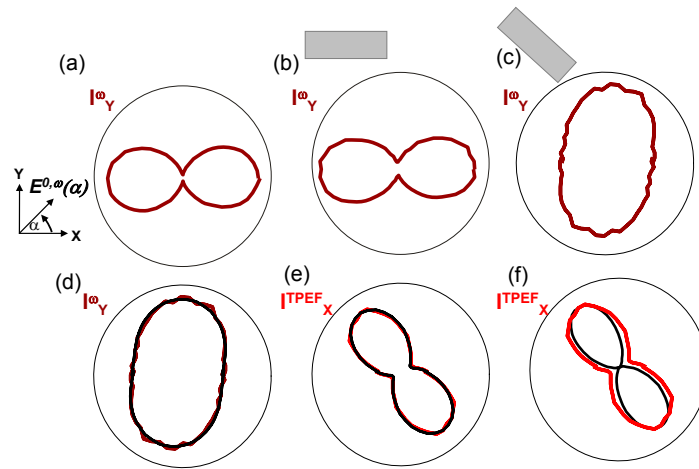


Fig. 4. Experimental birefringence and TPEF polarimetric measurements in a PHTP-DANS 1D crystal. (a) Laser polarimetric response I_Y^ω of the non-birefringent glass substrate (no crystal). (b,c) Laser polarimetric response through the crystal oriented along the (b) X axis and (c) tilted at about 135° relative to X (as sketched). (d) Fit of the laser polarimetric response (solutions : $\Theta_b = 138^\circ$, $\Phi_b = 116^\circ$). (e) Fit of the TPEF I_X^{TPEF} polarimetric response including birefringence, at a $5 \mu\text{m}$ penetration depth (solutions : $\varphi_0 = 164^\circ$, $\Theta_b = 138^\circ$, $\Phi_b = 100^\circ$). (f) Fit of the TPEF polarimetric response with no birefringence included. All the fits include the dichroism and ellipticity parameters of the dichroic mirror (dichroism $\gamma = 0.009$, ellipticity factor $\delta = 13^\circ$ with the mirror used for this experiment [29]).

5. SHG polarization resolved microscopy in collagen

In this part the effect of birefringence is explored on the SHG polarimetric data on collagen type I fibers from rat-tail tendons, attached at both ends on a coverslip and immersed in 0.15M NaCl. To prepare the fibers, Adult Sprague Dawley rats were euthanased for purposes unconnected with the present research. Tails were removed and immediately snap frozen in liquid nitrogen cooled isopentane. At the time of use the tissue was thawed and the tendon exposed. Individual fibers were teased out by microdissection and either examined immediately or stored frozen until required. Control Raman spectra were identical in either case, contained none of the peaks characteristic of proteoglycans, and were indistinguishable from those obtained from fibers purified by enzymatic extraction.

SHG imaging has been widely studied on similar systems. Analysis of SHG polarization resolved experiments is traditionally done assuming the collagen fibers to be of C_6 symmetry, equivalent to considering a collection of nonlinear individual dipoles within a cone distribution of typical half apertures angles ranging from 50° to 65° [15, 16, 18, 21, 22]. Calculated SHG polarimetric responses are depicted in Fig. 5(a) for different tilt angle φ_0 of theoretical collagen fibers. The effect of a theoretical birefringence is seen to be detrimental to the polarimetric responses, introducing extra lobes in the polar plot shape comparing to the absence of birefringence. Again in this case, analyzing SHG polarimetry not accounting for birefringence leads to erroneous tensorial analysis of the SHG response.

Experimental analyzes performed in collagen type I fibers of thickness ranging from $70\mu\text{m}$ to $100\mu\text{m}$ confirm the strong deformation induced on the polarimetric responses, even for a few μm penetration depths in the sample [Fig. 6(a)–6(c)]. In a fiber close to horizontal along

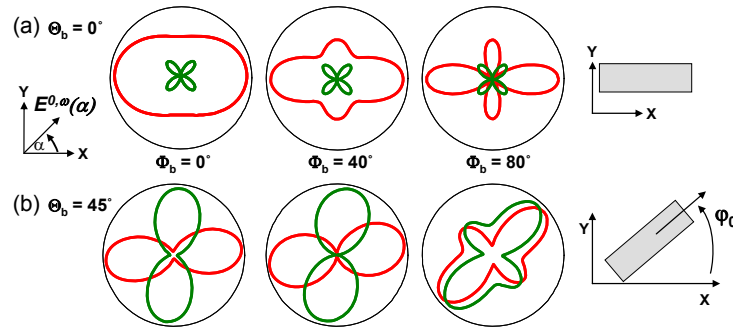


Fig. 5. Theoretical SHG polarimetric responses (I_X^{SHG} (red) and I_Y^{SHG} (green)) for a collagen fiber which nonlinear tensor corresponds to a cone half angle aperture distribution of the nonlinear molecular dipoles of 50° . The orientation of the fiber φ_0 also corresponds to the optical axis orientation Θ_b . (a) $\varphi_0 = \Theta_b = 0^\circ$ and (b) $\varphi_0 = \Theta_b = 45^\circ$, with different values of the birefringence phase shift Φ_b .

the X direction, two lobes appear clearly in the I_X^{SHG} polarimetric response, that cannot be explained in the absence of birefringence. The fit of the I_X^ω response [Fig. 6(d)] confirms that the birefringence originates from a uni-axial system oriented close to the X axis ($\Theta_b = 18^\circ$), with a phase shift $\Phi_b = 119^\circ$. This birefringence is consistent with $\Delta n \approx 0.003$ [37, 38] in a $\approx 88\mu\text{m}$ thick fiber. The fitting of the SHG polarimetric responses at different penetration depths are performed using Θ_b and Φ_b as fitting parameters for both I_X and I_Y . Excellent fitting quality is obtained for a cone distribution of 52° half aperture angle, oriented at $\varphi_0 = 10^\circ$, which corresponds to the fiber direction observed in the SHG image (Fig. 6). The SHG fitting results show that the orientation of the optical axis $\Theta_b = 2 - 9^\circ$, measured locally, lies close to φ_0 . The difference with the averaged $\Theta_b = 18^\circ$ measured over the whole sample thickness is most probably due to the sample heterogeneity in the Z propagation direction. At last, the measured birefringence phase shifts increase when further penetrating in the sample, as expected. Supposing a birefringence $\Delta n \approx 0.003$, the deduced theoretical penetration depth (see values in brackets given in the Fig. 6 legend) are consistent with the expected depths of focus d , including error margins due to the focal volume averaging over several micrometers in the Z direction.

In the data shown in Fig. 6, the direction of the optical axis Θ_b , measured locally, is still relatively close to its averaged value over the whole sample thickness. This is not always the case as shown in another area of the same sample (Fig. 7). In this situation the SHG polarimetric fit gives $\Theta_b = (-23^\circ) - (-12^\circ)$ in the explored depths of focus [with consistent birefringence phase shifts, see Fig. 7(a)–7(c)], whereas $\Theta_b = 36^\circ \equiv (-54^\circ)$ on average. This is a clear signature of a progressive rotation of the collagen fiber / optical axes orientation when penetrating in the sample depth. Note that still accounting for the variations of φ_0 seen on the SHG images does not notably change these results.

These results show finally, that particular care has to be brought on the local properties of the sample, which can be very distinct from averaged birefringence since the optical axis of the system can typically rotate progressively through the whole sample thickness. At last, a complete fitting procedure on both the cone shape and birefringence parameters at each measurement point is therefore necessary to lead to reliable data on the nonlinear tensor of the structure. These experimental SHG polarimetric data, performed at distances still relatively close to the sample surface, indeed clearly evidence the presence of birefringence and demonstrate the im-

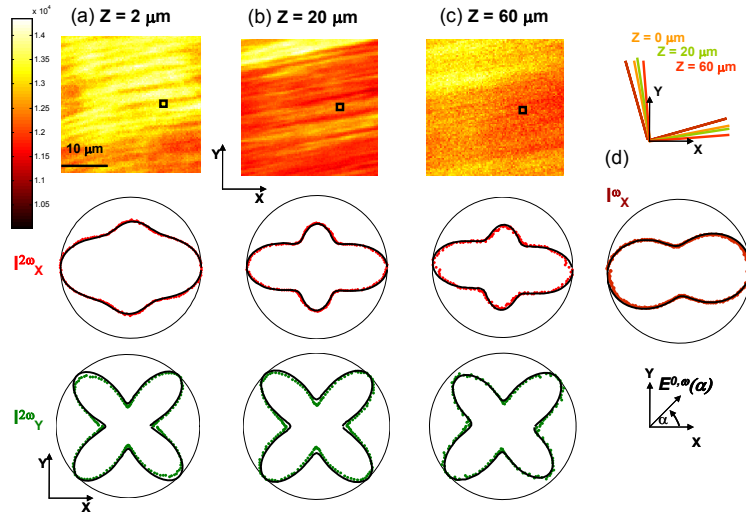


Fig. 6. Experimental SHG polarimetric responses for collagen type I fibers oriented close to the macroscopic X axis. The SHG images (image scale is in counts/s) represent a $30\mu\text{m}\times 30\mu\text{m}$ area of the sample scanned at different depth d : (a) $2\mu\text{m}$, (b) $20\mu\text{m}$, (c) $60\mu\text{m}$. Both SHG experimental intensities I_X (red dots) and I_Y (green dots) are depicted (after normalization for more visibility), together with the corresponding fit according to the model detailed in the text. The parameters obtained from the fits are 52° and $\varphi_0 = 10^\circ$ for respectively the cone distribution orientation and aperture, and : (a) $\Theta_b = 7^\circ$, $\Phi_b = 19^\circ$ [$14\mu\text{m}$];(b) $\Theta_b = 9^\circ$, $\Phi_b = 29^\circ$ [$22\mu\text{m}$];(c) $\Theta_b = 2^\circ$, $\Phi_b = 88^\circ$ [$65\mu\text{m}$]. (d) Birefringence measurement and fit on the I_X^ω component of the incident field, leading to birefringence parameters of $\Theta_b = 18^\circ$, $\Phi_b = 119^\circ$ [$88\mu\text{m}$], when the sample is propagated through. The found birefringence axes are represented in the inset scheme.

portance of accounting for such effect to retrieve sample structural information.

6. Conclusion

We have demonstrated that birefringence from molecular and biological samples is a detrimental factor in polarization resolved information in microscopy imaging applied to anisotropic samples. We have shown that this birefringence can be however fully characterized and accounted for. In a context where SHG microscopy constantly evolves towards the exploration of complex tissues where birefringence is present at increasing depths, this analysis is more and more crucial to distinguish the local nature (symmetry, orientational disorder) of molecular and biomolecular assemblies. This study can be extended to other contrasts such as Third Harmonic Generation (THG) or Coherent Anti-Stokes Raman Scattering (CARS) for which polarization-resolved microscopy has also been implemented.

Acknowledgements

We thank Prof. C. Peter Winlove (Biomedical Physics Group, University of Exeter) for providing the collagen Type I sample. We thank Patrick Ferrand and Hervé Rigneault for help in the experimental setup development and useful discussions. The authors acknowledge the European Commission through the Human Potential Program (Marie-Curie Research Training Network NANOMATCH, contract MRTN-CT-2006-035884). This work is also supported by the French Agence Nationale de la Recherche under the program ANR JC 2007, project

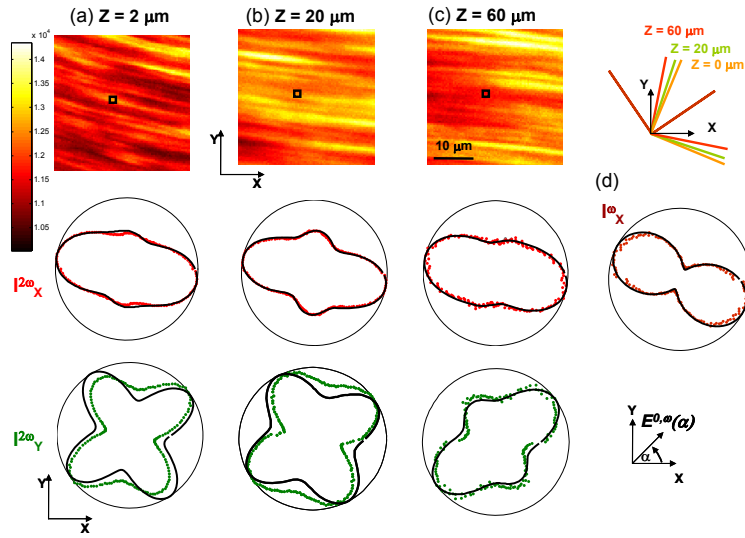


Fig. 7. Experimental SHG polarimetric responses for collagen type I fibers oriented at about 45° relative to the macroscopic X axis. The experimental parameters are the same as in Fig. 6. The corresponding birefringence parameters obtained from the fits are 52° and $\varphi_0 = -15^\circ$ for respectively the cone distribution orientation and aperture, and in addition: (a) $\Theta_b = -23^\circ$, $\Phi_b = 4^\circ [4\mu\text{m}]$; (b) $\Theta_b = -16^\circ$, $\Phi_b = 13^\circ [11\mu\text{m}]$; (c) $\Theta_b = -12^\circ$, $\Phi_b = 75^\circ [64\mu\text{m}]$. (d) Birefringence measurement and fit on the I_X^0 component of the incident field, leading to birefringence parameters of $\Theta_b = 36^\circ$, $\Phi_b = 115^\circ [85\mu\text{m}]$, when the sample is propagated through. The found birefringence axes are represented in the inset scheme.

NLO-Shaping JC07-195504.